Optical Engineering 53(3), 033111 (March 2014)

Detailed experimental characterization of reflectance spectra of *Sasakia charonda* butterfly using multispectral optical imaging

José M. Medina,[a,*] **José A. Díaz,**[a,*] **Eva Valero,**[a] **Juan L. Nieves,**[a] **and Pete Vukusic**[b]
[a]Universidad de Granada, Facultad de Ciencias, Departmento de Óptica, Edificio Mecenas, 18071, Granada, Spain
[b]University of Exeter, School of Physics, Exeter EX4 4QL, UK

Abstract. A multispectral acquisition system to examine the bidirectional reflectance distribution function of structurally colored biological materials in the visible range is presented. We focus on the purple-blue and white-pearl wing scales of the male butterfly *Sasakia charonda*. Multispectral imaging was done by changing the illumination angular position around the sample as well as that of the specimen around the multispectral sensor axis. Reflectance spectra were transformed to color coordinates and visualized in different color spaces. Spectral analysis shows distinct iridescent patterns in purple-blue and white-pearl scales. Colorimetric analysis indicates that purple-blue scales enhance blue coloring and exhibit higher color saturation. Principal component analysis reveals that the number of principal components that account for more than 99% of reflectance variability was higher in white-pearl scales. This suggests a higher spectral complexity in their spatial color pattern formation. Reconstruction of reflectance spectra from the principal components is discussed. We conclude that multispectral imaging provides new insights into spatial reflectance mapping that result from the combination of structural colorations and variable amounts of absorption pigments. *© 2014 Society of Photo-Optical Instrumentation Engineers (SPIE)* [DOI: 10.1117/1.OE.53.3.033111]

Keywords: biology; iridescence; color signaling; multispectral imaging; image analysis; reflectance; multilayers; melanin pigment.

Paper 131912 received Dec. 19, 2013; revised manuscript received Feb. 23, 2014; accepted for publication Feb. 28, 2014; published online Mar. 31, 2014.

1 Introduction

Iridescent colors are ubiquitous in biological systems. They are associated with many animal appearances, such as those arising from peacock feathers, beetle elytra, and moth and butterfly scales. The iridescent reflectances of many species of lepidopteran wings are created by the combination of selective light absorption by pigments and the coherent scattering from periodic micron and submicron components of the scales.[1–3] Morphologically, some examples of iridescent scales have a characteristic structure, sometimes referred to as the *Morpho*-type structure.[4] This features a lower single membrane on which discrete ridges sit, running in parallel to the long axis of the scale. The ridges themselves comprise lamellae of cuticle interspaced with air that, together, form discrete packets of stacked multilayers across the entire area of the scale.[1,5,6] The upper membrane can also exhibit microribs, or parallel columns oriented nearly perpendicular to the lamellae and transversal crossribs that connect the ridges between them.[2,3,5,7] In some species, the multilayer stacks can be slanted from the base plane to produce iridescence over a limited angular view.[3,8–12] Distinct ultraviolet UV-blue iridescent patterns in *Apaturinae* butterflies, a subfamily of the family Nymphalidae, originate from the tilted multilayer stacks on the ridges.[13–15]

The *Sasakia charonda* butterfly (*S. charonda*) is a species of *Apaturinae* (usually called "the great purple emperor").[12–14,16,17] The bright purple-blue and white-pearl iridescence in the male *S. charonda* are similar to the purple emperor butterflies *Apatura iris* (*A. iris*) and *Apatura ilia* (*A. ilia*).[15,18] Structural characterization using optical and high-resolution electron microscopy, described elsewhere, has concluded that ridges of the purple-blue and white-pearl scales are composed of seven cuticle-air lamella titled approximately 8 deg relative to the base of the wing scale.[12–15] The cross section of the central pillar of ridges exhibits a Christmas tree shape.[12–15,19] Such ridge-lamella structures have been analyzed in detail and reported in many lepidopteran wings such as in the *Ancyluris meliboeus*,[9] *Euploea mulciber*,[10,12] and in various *Morpho*,[2,6,18,20] and pierid butterfly species.[8,11]

Iridescent reflection in the *S. charonda* wing scales is produced by coherent scattering of light at short wavelengths between 200 and 450 nm.[12–14] In comparison to *A. meliboeus*[9] and *E. mulciber*,[10,12] iridescent reflection in *S. charonda* occurs over a wider angular range in the observation hemisphere of wing scales, with an angular portion that does not exhibit iridescence (i.e., a "dark zone")[9] of 16 deg.[12–14] Purple-blue and white-pearl scales have the same structure and the differences are ascribed to differences in their content of melanin.[13,14] Melanin is a common absorption pigment found in nature (e.g., human hair, skin, etc.).[21] Purple-blue scales have been shown to have higher melanin content; they produce vivid iridescence under light reflection, and they appear dark brown under light transmission. In contrast, the white-pearl scales contain less melanin: hence the reflected light appears whitish and they are nearly transparent under light transmission.[12–14] The effect of

---

[*]Address all correspondence to: José M. Medina, E-mail: jmedinaru@cofis.es; José A. Díaz, E-mail: jadiaz@ugr.es

melanin in the wing scales is important because it may enhance the directional UV-blue iridescence from cuticle-air stacks on the ridges by absorbing undesirable background scattering in the green and yellow regions, in a similar way as in various *Morpho* species.[2,6,22] Figure 1 summarizes the different structures of the *S. charonda*.

Although detailed structural characterization of the *S. charonda* has been investigated before,[12–14,16] a lack of information persists concerning its optical properties. Particularly, the quantification of the reflectance spectra and its possible dependency with the illumination geometry deserves study. The complete characterization of the reflectance spectra in structurally colored biological materials requires the determination of the bidirectional reflectance distribution function (BRDF).[23,24] The BRDF is defined as the ratio of the reflected spectral radiance to the incident spectral irradiance as a function of the illumination and detector angular positions.[23,24] Determination of the BRDF is often slow and cumbersome to obtain, and it generates a large quantity of spectral data. Therefore, the BRDF is usually simplified by measuring the reflectance spectrum at few angles of illumination and detection positions.[2,3,24] BRDF data have been extensively discussed in single wing scales[6,24–27] and in spatially extended wing areas.[2,3,10,11,15,24] However, this is done usually without consideration of the spatial arrangement of wing scales. Measurement of the BRDF at different locations is important to understand how spatial periodicity, defects, and disorder of wing scales affect the color mixing effects and may help in the artificial replication of bioinspired structures.[1–3] In a different type of application, the measurement of the BRDF in structurally colored butterflies is important in computer graphics rendering.[25,28,29]

Multispectral imaging offers a plausible nondestructive solution to spatial reflectance mapping by the combination of spectroscopic and digital image analysis of distant surfaces with high spatial resolution. Multispectral imaging provides thousands of reflectances, i.e., one per pixel at every location of the captured scene, and it involves the generation of a three-dimensional (3-D) data cube or "image cube,"[30] with two spatial dimensions, or the x, y plane, the size of the digital image, and the third, the spectral axis, sampled over a discrete number of wavelength intervals.[30–33] Multispectral imaging can complement other spectrophotometric methods,[3,24,26,27] providing valuable information of the spatial distribution of iridescence at the distance of a few microns.[34] The micro-appearance of butterfly wings changes from place to place[2] and varies markedly with the illumination and viewing angles. This arises due to sample imperfections and the manner in which wing veins and scales are spatially distributed, their relative orientations and surface roughness. Given these complicating factors, it would be useful to measure the multispectral BRDF of distinct wing areas at the micron scale.

The aim of the present study is to investigate the reflectance of the purple-blue and white-pearl wing scales of the *S. charonda* butterfly by measuring their multispectral BRDFs. Although various multispectral systems have reported capabilities of acquiring BRDFs of isotropic reflective materials,[35–37] they have not focused on the properties of iridescent biological systems. Structurally colored butterflies are usually anisotropically reflecting systems.[2,20] We have examined reflectance spectra in the visible range as a function of the illumination angle from near to far from surface normal. The BRDF can also be measured over a wide range of spatial positions by rotating the butterfly wing around the multispectral sensor axis. We have compared the iridescent purple-blue and white-pearl effects at different orientations of the wing scales. Spectral correlation analysis of the multispectral BRDF data was done by applying principal component analysis (PCA).[32,38–40] PCA is a standard statistical method in remote sensing and multispectral analysis[32,40] and in color technology[39,41] that reduces a high-dimensional set of variables into a low-dimensional one.[32,40] Variation in high-dimensional data sets can be assessed by the covariance matrix. PCA is usually performed on the covariance matrix and decomposes reflectance spectra into a linear combination of few orthogonal vectors (usually called eigenvectors). The goal of PCA is to preserve as much variation as possible of the original data set. Variance correlates with the eigenvalues of the covariance matrix. Eigenvectors and eigenvalues of the covariance matrix are always in pairs so that eigenvectors are often sorted according to the decreasing eigenvalues. Therefore, the largest variance is associated with the first eigenvector. The second largest variance is associated with the second eigenvector and so on.[32,38–40] In previous works, PCA has been used to examine the reflectance spectra of *Morpho* butterflies in a low-dimensional space when exposed to different liquids[42] and vapors,[43,44] and in models of the distribution of eigenvalues.[45] In the present study, we have applied the PCA to multispectral BRDF data in a different way, i.e., to examine the spectral pattern formation by the wing scales at different spatial locations in the wing. First, we have compared the spectral bands of the purple-blue and white-pearl eigenvectors. We also have examined the possible influence of the illumination angle by comparing the extracted eigenvectors from near to far from surface normal. Finally, we have examined the reconstruction of the reflectance spectra from PCA using a varying number of eigenvectors for interpretation of the data.[32,38–40] This also allows us to characterize the extent of reflectance variability in the spatial color mosaic produced by the purple-blue and white-pearl wing scales.

2 Methods

2.1 *Structural Characterization*

Structural analysis (Fig. 1) was undertaken by means of optical and scanning electron microscopy (SEM). Optical images of the entire butterfly wing [Fig. 1(a)] were captured with a conventional digital color camera Canon PowerShot SD1000. Reflection color photomicrographs were obtained by using an optical microscope Nikon Optiphot-100 connected to a charge coupled device (CCD) color video camera Sony DXC-107AP [Fig. 1(b)], and transmission ones by using an optical microscope Olympus BX51 with a DP50 digital camera [Fig. 1(c)]. A SEM micrograph of a small bluish region of the specimen forewing was obtained [Fig. 1(d)]. For this, it was coated with a thin film of gold palladium alloy (80 to 20 wt. %) by using a sputter coater 208HR Cressington coupled to a thickness controller MTM-20 Cressington and examined by using a NOVA 200 Nano SEM FEI instrument.

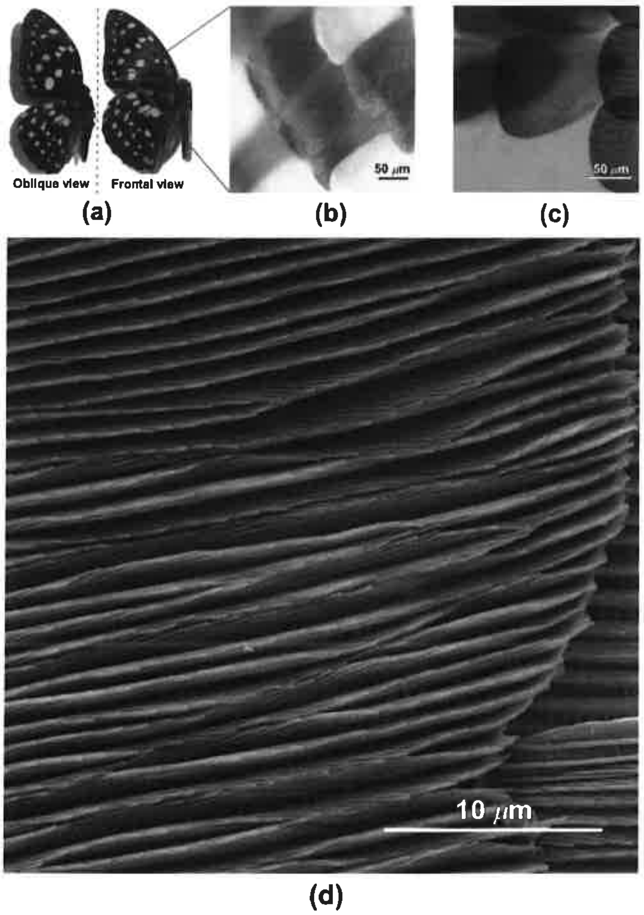

Fig. 1 (a) Optical image of fore and hind wings from a male *S. charonda* butterfly at different viewing angles. (b and c) Reflection optical micrograph (20×) and transmission optical micrograph (60×) of the purple-blue and white-pearl iridescent wing scales, respectively. (d) Scanning electron microscope micrograph (10,000×) of a purple-blue iridescent wing scale. The top view of the wing scale affords us to observe the cuticles piled over the ridges.

2.2 *Multispectral Imaging Setup*

The experimental setup is represented in Fig. 2. The multispectral sensor comprised a liquid crystal tunable filter (LCTF) (Varispec VS-VIS2-10HC-35-SQ) placed in front of a conventional objective zoom lens (Navitar Zoom 7000 18: 108 mm) attached to a 12-bit monochrome CCD (Retiga QImaging SVR1394).[46] The LCTF, zoom lens, and CCD sensor array were in a fixed position and they were exactly aligned perpendicular to a male *S. charonda* forewing (Fig. 2).

The LCTF is based on a Lyot-Ohman filter configuration that provides spectral tuning and modulates spectral transmittance electronically.[30,31,47] The LCTF has a 35-mm aperture, a field of view of 7.5 deg, and a full bandwidth at half maximum that is not constant, but varies from 7 to 15 nm depending on the working wavelength. The CCD camera captures digital images having 1392×1040 pixels each with a size of 6.45×6.45 μm.[46] The CCD camera and the LCTF have been fully tested in multispectral data collection from skylight imaging in our laboratory.[46] The illumination system uses a 150 W highly stable mercury xenon (Hg-Xe) lamp (Hamamatsu L9588-04) coupled to a 1.5 m flexible fiber light guide mounted in a goniometric setup. This light guide has a condenser lens with a focal length of 50 mm. At the distance of 20 cm perpendicular to the imaged scene, the light guide provides a squared area of 40 mm high by 40 mm wide of uniform light. The light guide and the condenser lens were placed in a 360-deg continuous rotation stage having a positional resolution of 1 deg. The illumination angular position is measured from the surface normal and it is denoted by the angle θ.

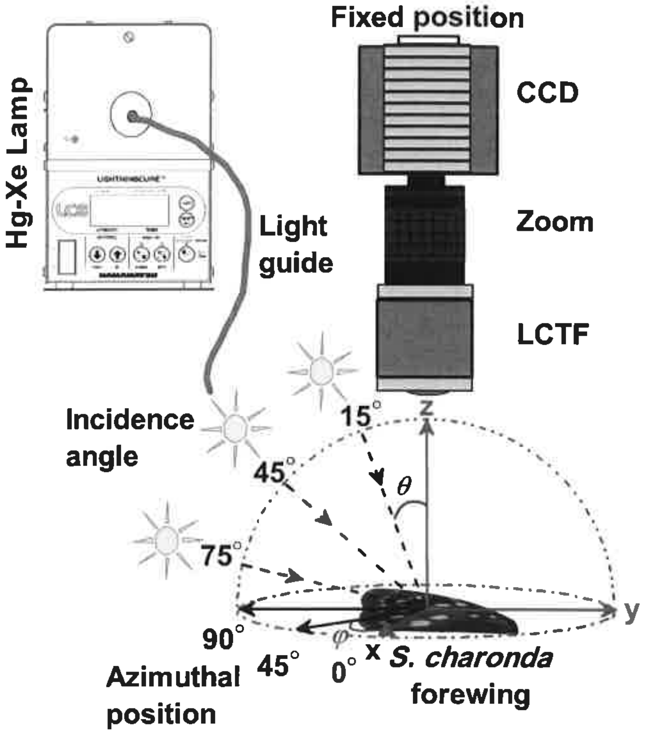

Fig. 2 Schematic representation of the multispectral imaging setup. The CCD camera, zoom lens, and the LCTF are in a fixed position perpendicular to *S. charonda* forewing. The light guide was rotated from near to far from surface normal at the illumination angles θ of 15, 45, and 75 deg. The specimen was rotated around the multispectral sensor axis (z-axis) at the azimuthal angles φ of 0, 45, and 90 deg. See text for details.

We measure reflectance from the *S. charonda* butterfly at the θ values: 15, 45, and 75 deg (Fig. 2). Note that when θ is 45 deg, the experimental setup reproduces the standard measurement geometry for diffuse reflectance CIE 45 :0 (*Commission Internationale de l'Éclairage*).[34,48,49] The *S. charonda* forewing was mounted in a 25.4-mm-diameter hole of a continuous rotation stage. The sample was fixed on the rotation stage using tiny strips of Parafilm at the borders. Flatness was achieved by adjusting the strips. The hole guarantees an effective nonscattering background in the field of view of the multispectral system.[34] The rotation stage enables a rotation of the butterfly wing manually around the observation axis. The azimuth angular position is defined in the x, y-plane with respect to x-axis, and it is denoted by the angle φ (Fig. 2). We rotate the butterfly sample at the φ angles: 0, 45, and 90 deg. Therefore, multispectral BRDF data were sampled at three values of θ and φ providing nine different angular configurations (Fig. 2): $(\theta, \varphi) = (15\text{ deg}, 0\text{ deg})$; (15 deg, 45 deg); (15 deg, 90 deg); (45 deg, 0 deg); (45 deg, 45 deg); (45 deg, 90 deg);(75 deg, 0 deg); (75 deg, 45 deg); (75 deg, 90 deg).

2.3 *Experimental Procedure*

To guarantee stability in the illumination source, multispectral measurements were started after it was turned on for a minimum of 5 min. Multispectral data collection was controlled by using custom software in a dark room. The software allows the LCTF to be tuned from 400 to 700 nm in steps of 10 nm giving a total of 31 different spectral bands in each image cube. The software also calculated the exposure time at each wavelength automatically by taking into account that the number of digital counts was within 85% of the CCD saturation level at any pixel in the image cube. The chromatic aberration was compensated for by manually focusing the zoom lens.[48] The spectral reflectance factor is often defined as the ratio of the spectral flux reflected by a test sample to the spectral flux reflected by a white diffuse reflectance standard (Lambertian) at a specific wavelength.[48] The spectral reflectance factor of the *S. charonda* in the visible spectrum was reconstructed by using a linear response model of monochrome CCD sensors.[30–32,34,50] White and zero reflectance calibration were performed by using the two-point correction method:[30–32]

$$R_{i,j}(\lambda) = \rho \frac{I_{i,j}(\lambda) - O_{i,j}(\lambda)}{W_{i,j}(\lambda) - O_{i,j}(\lambda)}, \tag{1}$$

where $R_{i,j}(\lambda)$ and $I_{i,j}(\lambda)$ denote the spectral reflectance factor and the collected multispectral sensor response of the *S. charonda* at the pixel positions i, j, respectively. The white flat field $W_{i,j}(\lambda)$ gives a measure of the white reference.[30–32,50] This was obtained at each illumination angle from a 99% white diffuse reflectance Spectralon standard.[51] In all cases, the Spectralon sample was defocused with the zoom lens to avoid spatial noise from the nonhomogeneous structure under high magnification.[32] The dark field $O_{i,j}(\lambda)$ gives a measure of the CCD dark current response.[30–32,50,52] It was obtained in the same conditions as in the white flat field but without the sample holder, with the light source off and in a dark room, thus preventing any residual light from reaching the CCD camera. The normalization factor ρ gives the Spectralon correction for nearly Lambertian surfaces,[30,32] and it was obtained from the manufacturer tabulated data.[51] The multispectral optical imaging arrangement had a spatial resolution of 14.4 μm/pixels at the sample distance. To minimize spatial nonuniform effects from the CCD sensor[46] and LCTF, an image square of 400×400 pixels was selected at the center of the captured image cube.[34]

2.4 *Colorimetric Performance*

The colorimetric analysis and methods employed here are standard and they are described in detail elsewhere.[25,34,48] The CIE XYZ tristimulus values were calculated from the reflectance data by using the CIE 1931 2-deg color matching functions, $\bar{x}(\lambda)$, $\bar{y}(\lambda)$, $\bar{z}(\lambda)$ and the CIE standard illuminant D65 to simulate daylight conditions.[48,49] This illuminant was used hereafter in all colorimetric calculations. First, the XYZ tristimulus values were converted to the standard red, green, and blue color spaces (sRGB).[53] This color space is intended for color visualization in conventional displays.[53] XYZ tristimulus values were also converted into the CIE 1976 $L * a * b*$ color space (CIELAB) for further colorimetric analysis. The CIELAB color space is recommended for color representation of pigmented thin films.[48,49] $L*$, $a*$, and $b*$ are the lightness, red-green, and blue-yellow orthogonal axes, respectively. The $a*$, $b*$ color plane indicates the red ($a* > 0$), green ($a* < 0$), blue ($b* < 0$), and yellow ($b* > 0$) coordinates whereas is the perpendicular achromatic axis ($L* > 0$).[48,49] The chroma value $C^*_{ab} = (a *^2 + b*^2)^{1/2}$ is often used in the industrial color evaluation for both light absorption and special effect pigments, and it is related to saturation value.[48,49] Saturation is an attribute that expresses the colorfulness of colorants and it does not necessary imply an increase of colorant concentration. High chroma values indicate high saturation and gain of colorfulness and vice versa.[48,49] The projection of color effects in the $a*$, $b*$ plane at specific illumination and viewing angles is a useful method for characterizing special effect pigments.[49] Thus, the change of lightness is not considered and the projection in the $a*$, $b*$ plane provides an overall fingerprint of the anisotropic color development of special effect pigments.[49] We have used a similar method in the colorimetric evaluation of several butterfly species' wing scales[34] by projecting in the $a*$, $b*$ plane the color coordinates that result from purple-blue and white-pearl wing scales[12–14] at different values of θ and φ.

2.5 *Spectral Calibration*

Calibration of the spectral transmittance of the LCTF has previously been performed in our laboratory.[46] Spectral calibration of the multispectral setup was done by retrieving the reflectance of several color patches of the Macbeth Color Checker chart.[31,32,54,55] The Macbeth chart is a popular training color dataset used in multispectral and color imaging formed by different color patches of known color pigments.[54] Their spectral properties, particularly their reflectance curves, are available elsewhere.[54,55] The Macbeth chart was illuminated at 45 deg which is equivalent to the CIE 45 :0 measuring geometry in spectrophotometry[48,49] (Fig. 2). Figure 3 shows the mean spectral reflectance factor of four representative Macbeth color patches obtained by the multispectral setup and that obtained by standard spectrophotometry.[55] Each mean spectral reflectance factor was averaged over the 1.6×10^5 sample area reflectance data. Note that the reflectances were normalized to the maximum value for comparison.

The multispectral imaging setup retrieves the shape of the reflectance curves of all Macbeth color patches but it was unexpectedly higher at low reflectance values around 400 nm. This is due to the low transmission efficiency of the LCTF[30,31,46] as well as the low response efficiency of the CCD sensor[50,52] at this working wavelength.

2.6 *Principal Component Analysis*

Reflectances at each pixel position were taken from 410 to 700 nm in 10-nm steps. Reflectance data at 400 nm were excluded in accordance with the previous spectral calibration analysis (Fig. 3). Therefore, reflectances were treated as 30-dimensional (30-D) vectors (i.e., as many dimensions as wavelength intervals) and they were arranged in a 2601×30 matrix with the reflectance vectors $\mathbf{R}_{i,j}$ in rows. PCA of reflectances was done by referring the reflectance spectra around the mean reflectance vector $\bar{\mathbf{R}}$. Each reflectance sample vector $\mathbf{R}_{i,j}$ in Eq. (1) was subtracted from $\bar{\mathbf{R}}$, $\mathbf{R}_{i,j} - \bar{\mathbf{R}}$. Then, the covariance matrix is computed

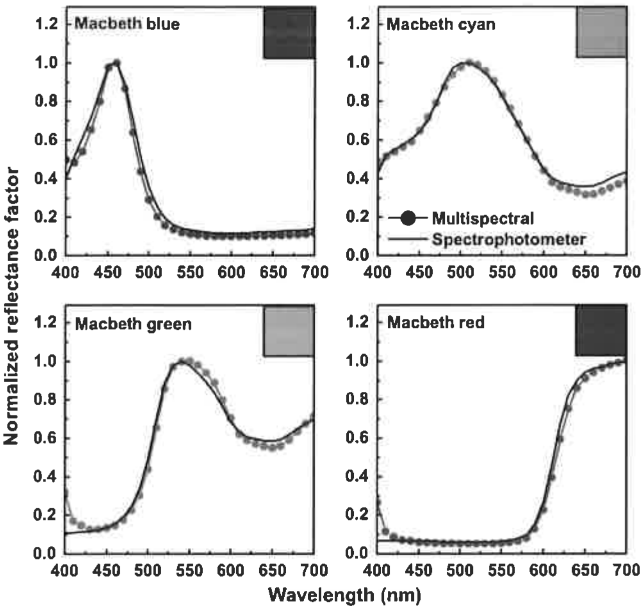

Fig. 3 Linear plot of the mean spectral reflectance factor averaged over 1.6×10^5 reflectances of four different blue, cyan, green, and red patches from the Macbeth Color Checker. Colored lines with symbols indicate the reflectance spectra recovered by the multispectral imaging setup at the angle $\theta = 45$ deg. Solid lines are the reflectance spectra provided by standard spectrophotometry. Reflectance data were normalized to their maximum values for comparisons. In each panel, the inset shows the corresponding color patch in the sRGB color space.

and the eigenvectors are extracted by diagonalization of the covariance matrix. Each reflectance sample $\mathbf{R}_{i,j}$ can be written as follows:[32,38–41]

$$\mathbf{R}_{i,j} = \bar{\mathbf{R}} + \sum_{k=1}^{30} \alpha_{i,j,k} \mathbf{S}_k. \tag{2}$$

The coefficients $\alpha_{i,j,k}$ are the coordinates or principal components[32,38–41] in the new reference system. $\mathbf{S}_k$ is the extracted eigenvectors or the new basis functions. In our case, the eigenvectors span a 30-D vector space, $k = 1, 2, \ldots, 30$ and they are orthogonal (perpendicular) to one another. The eigenvalues are the diagonal elements of the diagonalized covariance matrix in decreasing order and define the variances corresponding to the eigenvectors. The largest variance corresponds to the first eigenvalue and $\mathbf{S}_1$ is the associated eigenvector. The second largest variance corresponds to the second eigenvalue and its associated eigenvector $\mathbf{S}_2$ is perpendicular to $\mathbf{S}_1$ and so on. Therefore, those eigenvectors with associated low eigenvalues may be ignored in subsequent analyses. The normalized sum of eigenvalues up to a certain value of k is the cumulative variance accounting for the first k eigenvectors.[32,38–41]

Reconstruction of reflectance spectra was examined by taking Eq. (2). The goodness of fit between the original $\mathbf{R}_{i,j}$ and reconstructed reflectance sample vector $\mathbf{R}'_{i,j}$ at each pixel position was evaluated by using the root-mean-square (RMS) error:[39] $[\Sigma(\mathbf{R}_{i,j} - \mathbf{R}'_{i,j})^2]$. Color differences between the original and reconstructed purple-blue and white-pearl wing areas were done by mapping reflectance spectra at each pixel position to RGB color coordinates. Then, the color coordinates were transformed to a physiological color space of human cone photoreceptors, and the Spatial CIELAB (S-CIELAB) color difference formula was implemented.[56,57] The S-CIELAB color metric is an extension of the conventional CIELAB color difference formula ΔE[48,49] that includes an initial prefiltering stage to incorporate the spatial-color sensitivity of the human visual system.[56] Those S-CIELAB ΔE values less than the unity are often below the threshold and the color differences are not visually discernable.[56]

3 Results

3.1 *Spectral and Colorimetric Analysis*

Figure 4 shows in the sRGB color space the entire selected area of the *S. charonda* wing as a function of the illumination angle θ of 15, 45, and 75 deg and as a function of the azimuthal angle φ of 0, 45, and 90 deg. This gives a total of nine spatial color maps, i.e., color images, placed in a matrix arrangement of three rows by three columns. Each spatial color map consists of 400×400 pixels and covers an imaged area of 33.1 mm^2. Columns indicate a fixed value of φ, i.e., only the illumination angle θ is changed showing iridescence effects at a given orientation of wing scales. Rows indicate wing scales at different spatial orientations for a constant illumination angle θ. In all panels, black- and brown-lined features correspond to wing veins. Purple-blue color effects can be clearly observed across all panels except at the angles, $\varphi = 0$ deg and $\varphi = 45$ deg, both at the illumination angle, $\theta = 75$ deg. Color effects in these extended areas fade to dark brown because of the relative orientation distribution of wing scales that precludes iridescence. Then, only light diffused from melanin pigment is captured within the numerical aperture of the multispectral imaging system. At the angle φ of 0 and 45 deg, it is also possible to distinguish a white-pearl iridescent region. Note that both white-pearl areas at $\varphi = 0$ deg and $\varphi = 45$ deg correspond to the same region at different spatial positions and orientations. In each spatial color map, the squares mark different selected imaged areas of size 51×51 pixels (0.53 mm^2) at different spatial locations.

Figure 5 shows a semilogarithmic plot of the mean spectral reflectance factor of each selected area as a function of φ and θ. Each of the corresponding 18 mean reflectance values was obtained over 2601 reflectances in each selected square. In Fig. 5, mean reflectance values are grouped in six panels placed in a matrix arrangement of three rows by two columns. In each row, the azimuthal angle φ is fixed and each panel represents purple-blue or white-pearl iridescent effects of different imaged areas as a function of the illumination angle θ.

In purple-blue areas, the shape of the mean reflectance factor is similar to the reflectance spectra of the *A. iris* and *A. ilia* in the visible range as measured with conventional spectrometers.[15,19] The multispectral BRDF in Fig. 5 is sensitive to the surface roughness and the relative orientation of wing scales. In the purple-blue region at $\varphi = 90$ deg, the reflectance factor increases as the illumination angle changes for near to far from surface normal. The shape of the reflectance factor is similar except it shows a minimum at $\theta = 15$ deg and then it flattens for wavelengths higher than 480 nm as θ increases. The wavelength at which the reflectance factor is maximum (λ_{MAX}) shows null or poor dependency with the illumination angle θ. λ_{MAX} changes

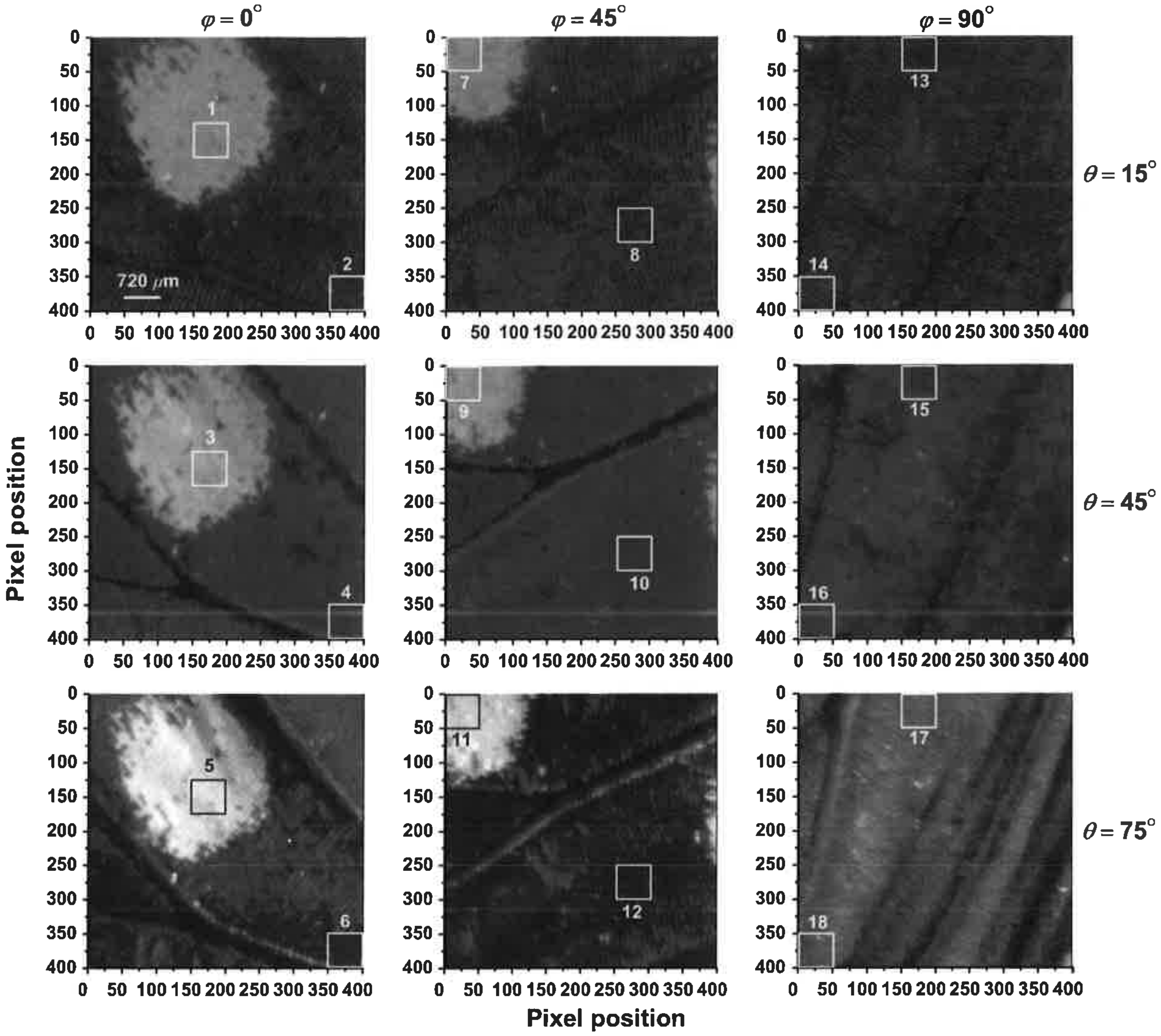

Fig. 4 Example of iridescence in the *S. charonda* butterfly. Spatial color maps in the sRGB color space (size 400 x 400 pixels) at the illumination angle θ of 15, 45, and 75 deg and at the azimuthal angle φ of 0, 45, and 90 deg. Open squares (size 51 x 51 pixels) labeled from "1" to "18" indicate different purple-blue and white-pearl regions at different spatial positions. Squares in the left column labeled as "1," "3," and "5" and "2," "4," and "6" indicate a white-pearl and a purple-blue iridescent area at the azimuthal angle φ of 0 deg, respectively. Those squares in the central column labeled as "7," "9," and "11" and "8," "10," and "12" correspond to a white-pearl and purple-blue regions at the azimuthal angle φ of 45 deg, respectively. In the right column, squares labeled as "13," "15," and "17" and "14," "16," and "18" show two different purple-blue iridescent regions at the angle φ of 90 deg, respectively.

from 400 to 410 nm at $\theta = 15$ deg to a maximum value of 430 nm at $\theta = 45$ deg (e.g., left-lower panel, squares 13, 15, and 17). At the azimuthal angle $\varphi = 0$ deg or $\varphi = 45$ deg, the spectral reflectance factor of purple-blue areas first increases between $\theta = 15$ deg and $\theta = 45$ deg and then it decreases at $\theta = 75$ deg showing a minimum. In the right-middle panel at $\varphi = 45$ deg (squares 8, 10, and 12), λ_{MAX} shifts from 400 to 410 nm at $\theta = 15$ deg to 700 nm at $\theta = 75$ deg. In this particular case, the mean spectral reflectance factor at 400 to 410 nm is very similar to that value at 700 nm promoting the visual perception of bluish-reddish or purple.[48]

In the white-pearl regions at $\varphi = 0$ deg (left-upper panel, squares 1, 3, and 5), the reflectance factor always increases as the angle θ changes for near to far from surface normal. The shape of the reflectance factor changes from bluish at $\theta = 15$ deg to a nearly white flat spectrum at $\theta = 75$ deg. λ_{MAX} shifts from 410 nm at $\theta = 15$ deg to 640 nm at $\theta = 75$ deg. A different effect is found in the same white-pearl region but now oriented at $\varphi = 45$ deg (left-middle panel, squares 7, 9, and 11). λ_{MAX} changes from 410 nm at $\theta = 15$ deg to 700 nm at $\theta = 75$ deg, the bluish part of the reflectance factor now decreases from $\theta = 15$ deg to $\theta = 75$ deg and weights the yellowish-reddish part of spectrum. Figure 6 shows the CIELAB color coordinates $(L*, a*, b*)$ of the 18 mean reflectance factors as a function of the illumination angle. CIELAB values are grouped in six panels placed in a matrix arrangement of three rows by two columns as in Fig. 5.

As expected, lightness values, $L*$, are higher for white-pearl wing scales whereas purple-blue wing scales often produce higher red, $(a* > 0)$, and blue, $(b* < 0)$. Different color

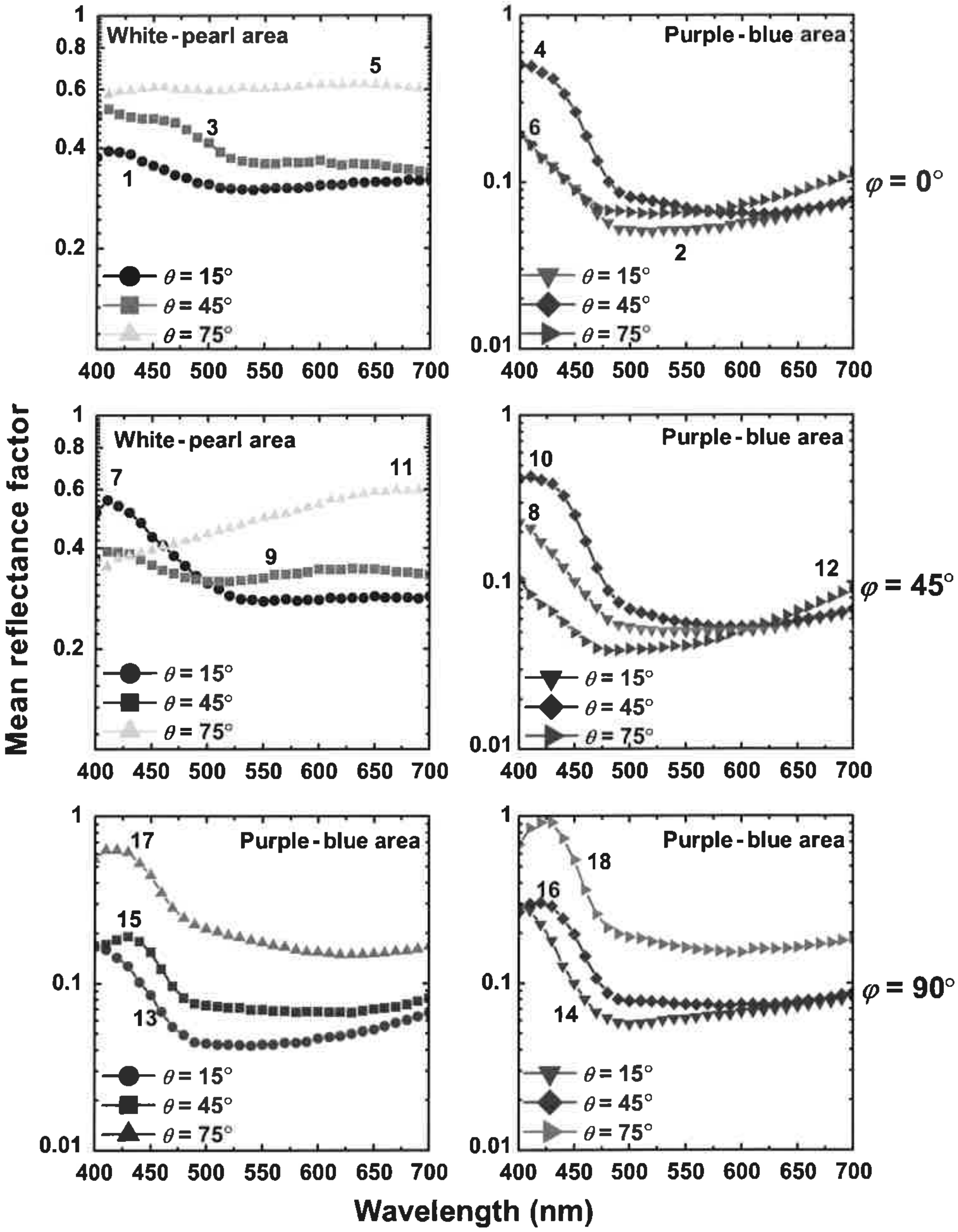

Fig. 5 Semilogarithmic plots of the mean spectral reflectance factor as a function of the illumination and the azimuthal angle. Numbers in each curve labeled from "1" to "18" indicate the spectral reflectance factor of each selected square region showed in Fig. 4. Each mean spectral reflectance factor was obtained from the average over 2601 reflectances.

patterns are observed as a function of φ and θ. At $\varphi = 90$ deg purple-blue wing scales exhibit higher lightness, red, and blue color coordinates as the illumination angle θ increases. At $\varphi = 45$ deg and $\varphi = 0$ deg, $L*$, $a*$, and $b*$ color coordinates increase from $\theta = 15$ deg to $\theta = 45$ deg and, then they decrease at $\theta = 75$ deg. At $\varphi = 45$ deg and $\varphi = 0$ deg in white-pearl wing scales, $L*$ always increases as the illumination angle θ increases. Chromaticity coordinates, $a*$ and $b*$, change from blue ($b* < 0$) and red ($a* > 0$) at $\theta = 15$ deg and $\theta = 45$ deg to yellow ($b* > 0$) and red ($a* > 0$) at $\theta = 75$ deg. Table 1 shows chroma values C^*_{ab} derived from the 18 mean reflectance values as a function of the azimuthal angle φ and the illumination angle θ.

Purple-blue chroma values, C^*_{ab}, are higher than white-pearl ones except at $\varphi = 45$ deg, $\theta = 75$ deg. Figure 7 shows in the $a*$, $b*$ color plane,[49] the projection of the angle-dependent color effects developed by the white-pearl and purple-blue wing scales.

Those $a*$, $b*$ coordinates in the vicinity of the achromatic point ($a* = 0$, $b* = 0$) correspond to "achromatic colors" (i.e., nearly white, gray, or black).[48,49] Two different and characteristic patterns result. Purple-blue wing scales exhibit color coordinates through one quadrant in the $a*$, $b*$ plane, i.e., in the reddish-bluish part ($a* > 0$, $b* < 0$). However, the color coordinates of white-pearl wing scales cluster near the achromatic point in two quadrants, i.e., reddish-bluish at $\varphi = 0$ deg ($a* > 0$, $b* < 0$) or reddish-yellowish ($a* > 0$.

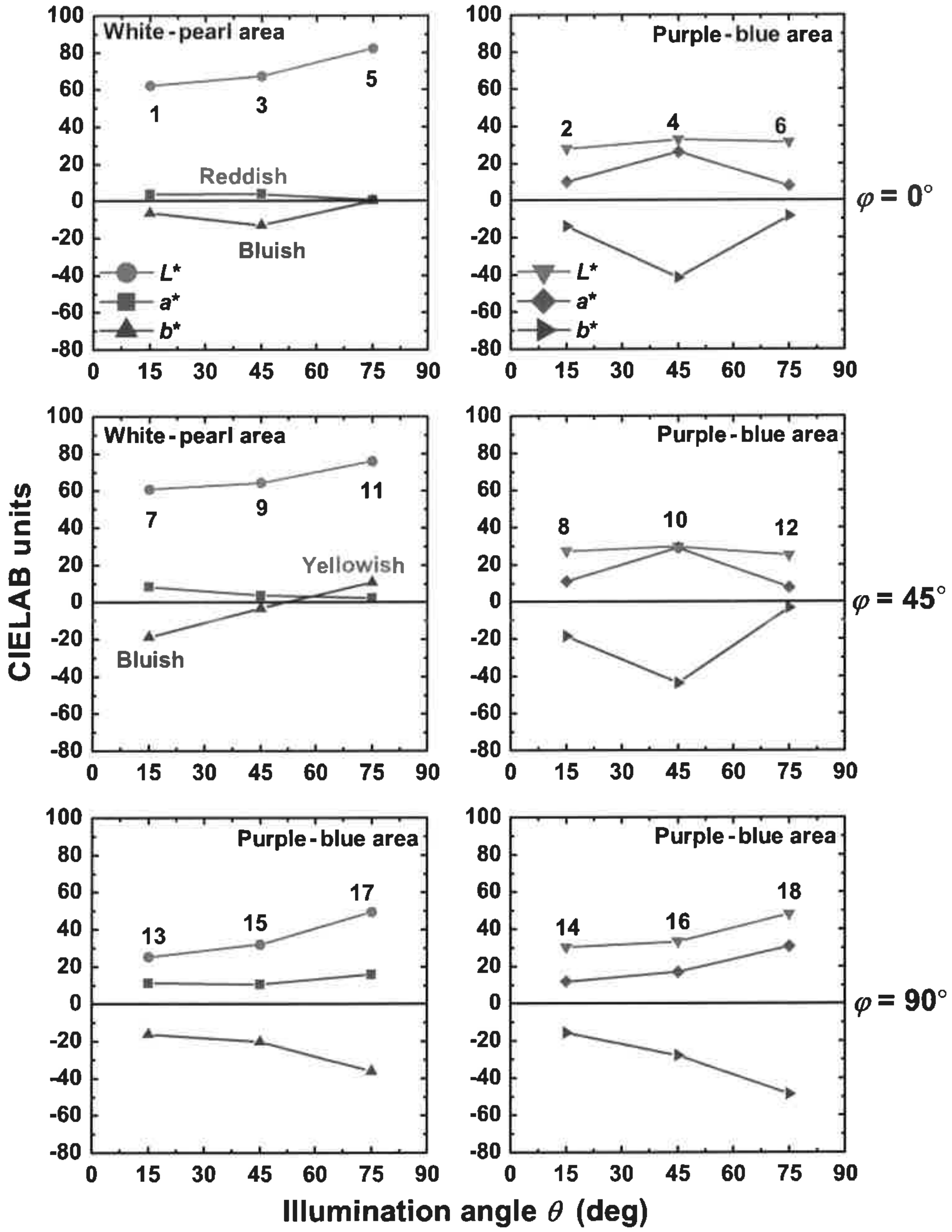

Fig. 6 Linear plots of the CIELAB values as a function of the illumination angle θ. Color coordinates were calculated by using mean spectral reflectance factors in Fig. 5, CIE 1931 color-matching functions of the 2-deg standard observer and CIE standard illuminant D65. At each illumination angle, numbers labeled from "1" to "18" indicate the color coordinates of each selected square regions shown in Fig. 4.

$b* > 0$) at $\varphi = 45$ deg. Therefore, Figs. 6 and 7, and Table 1 clearly indicate that purple-blue wing scales enhance the blue coloring and colorfulness.

3.2 *PCA of Reflectances*

PCA was done over 2601 reflectances at each of the 18 squares separately (Fig. 4). Spectral data at 400 nm were excluded (Fig. 3). It was necessary that the first six and the first 23 eigenvectors reach >99% of cumulative variance in purple-blue and white-pearl iridescent wing scales, respectively. Therefore, the original 30-D reflectance spectra can be simplified into a 6-dimensional and a 23-dimensional vector space in purple-blue and white-pearl scales, respectively, without much loss of variance. This also suggests that the spatial color formation of white-pearl scales contains more sources of spectral variability.

For instance, Fig. 8 compares the first four eigenvectors of purple-blue versus white-pearl wing scales at $\varphi = 0$ deg (squares 1, 3, and 5 and 2, 4, and 6, respectively, left column, Fig. 4). At this angle of the BRDF, the *S. charonda* exhibits the highest lightness, $L*$, values (Fig. 6). Weights or loadings[32,38–40] in Eq. (2) are grouped in 12 panels placed in a matrix arrangement of four rows by three columns. Each column indicates the eigenvectors or basis functions at the illumination angles of 15, 45, and 75 deg, separately. Note that the spectral shapes of eigenvectors in Fig. 8 are statistical values and have positive and negative values because the

Table 1 Chroma values C^*_{ab} of selected wing areas.

φ (deg)	θ (deg)	Purple-blue		White-pearl
	15	17		7.3
0	45	48.9		13.4
	75	11.5		1.2
	15	21.5		20.3
45	45	52.4		5.1
	75	8.6		11.5
	15	19.7	19.7	–
90	45	23	32.6	–
	75	39.3	57.5	–

reflectance spectra are subtracted from the sample mean reflectance [Eq. (2)].[32,38–41]

The first basis function has the largest eigenvalue and accounts for the majority of total variation of reflectance spectra; it is positive at all wavelengths and it is often interpreted as a measure of the overall direction along which reflectance spectra are distributed[32,38–40] (purple-blue, $\theta = 15$ deg, 47.5%, $\theta = 45$ deg, 71.5%, $\theta = 75$ deg, 87.6%; white-pearl, $\theta = 15$ deg, 48.9%, $\theta = 45$ deg, 62.5%, $\theta = 75$ deg, 72.6%). In the purple-blue wing scales, it weights all the spectral bands at $\theta = 15$ deg by approximately the same quantity. It has a small peak at around 650 to 660 nm at $\theta = 15$ deg, and then, it has a peak at 410 nm, at $\theta = 45$ deg and $\theta = 75$ deg. In the white-pearl wing scales, the basis function 1 broadens and has a small peak at 420 nm, at $\theta = 15$ deg. Then the peak shifts to 470 nm, at $\theta = 45$ deg, and finally, flattens at $\theta = 75$ deg. Similar angle-dependent effects on the basis functions have been found in multilayered interference reflectors.[58]

Basis function 2 indicates the second direction which reflectance spectra are distributed. It has the second largest eigenvalue and explains less variability in the reflectance spectra (purple-blue, $\theta = 15$ deg, 29.1%; $\theta = 45$ deg, 13.4%; $\theta = 75$ deg, 8.7%; white-pearl, $\theta = 15$ deg, 24.8%; $\theta = 45$ deg, 16.6%; and $\theta = 75$ deg, 15.6%). Basis functions 2 and 3 also modify their shape and shift in the horizontal wavelength axis as a function of the illumination angle θ in purple-blue wing scales but this effect is less evident in white-pearl scales. Differences between purple-blue and white-pearl wing scales are mainly located in the bluish-greenish-yellowish part of the spectrum, i.e., between 410 and 550 nm. In general, the shape of the white-pearl basis functions is similar to the purple-blue regions but the white-pearl eigenvectors broaden. The rest of eigenvectors, from the basis function 5 to the basis 30, weight different wavelength intervals and explain fewer spectral variations.[32,38–40]

3.3 *Reconstruction of Reflectance Spectra*

Reconstruction of reflectance spectra was done over 2601 reflectances in the selected purple-blue and white-pearl wing areas at the angular position $\varphi = 0$ deg and at the illumination angles $\theta = 45$ deg and $\theta = 75$ deg (Fig. 4). To examine the spectral variability of wing areas only in one direction of the 30-D space of reflectance vectors, each reflectance sample vector at each pixel position was projected by the linear combination of the mean reflectance $\bar{\mathbf{R}}$ and only one eigenvector $\mathbf{S}_k$, $\mathbf{R}'_{i,j,k} = \bar{\mathbf{R}} + \alpha_{i,j,k}\mathbf{S}_k$, $k = 1, 2, \ldots, 30$ [Eq. (2)]. Then the resulting reflectance spectra were mapped to color coordinates in the sRGB color space. For instance, Fig. 9 shows the projected reflectance spectra over the first four eigenvectors separately (see Fig. 8). The first row indicates the original purple-blue and white-pearl wing areas. The remaining rows represent the projected reflectance spectra in only one direction $\mathbf{S}_k$ ($k = 1, 2, 3, 4$). Therefore, each panel in Fig. 9 simulates hypothetical purple-blue and white-pearl wing scales

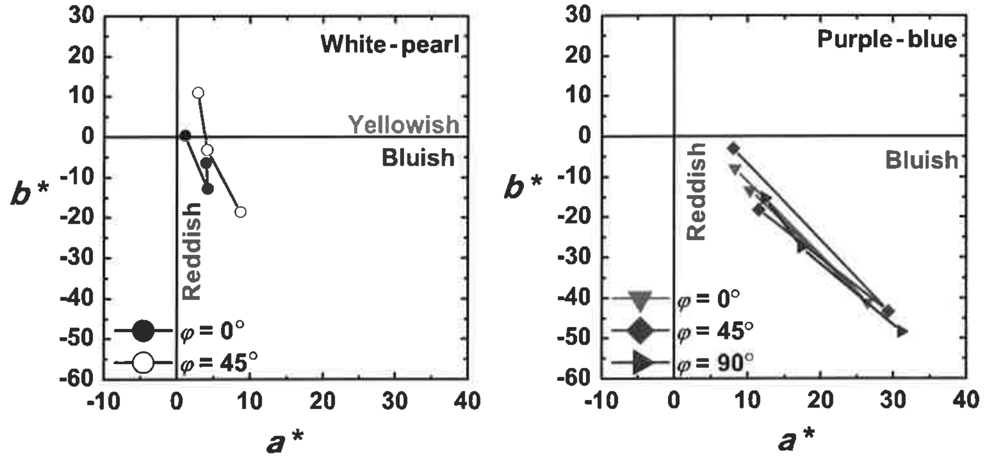

Fig. 7 Linear plots of the CIELAB $a*$, $b*$ color coordinates of the white-pearl and purple-blue wing scales. Color coordinates at different illumination angles are connected by solid lines and they are classified as a function of the azimuthal angle φ by using different symbols. Color coordinates were calculated by using mean spectral reflectance factors in Fig. 5, CIE 1931 color matching functions of the 2 deg standard observer and CIE standard illuminant D65.

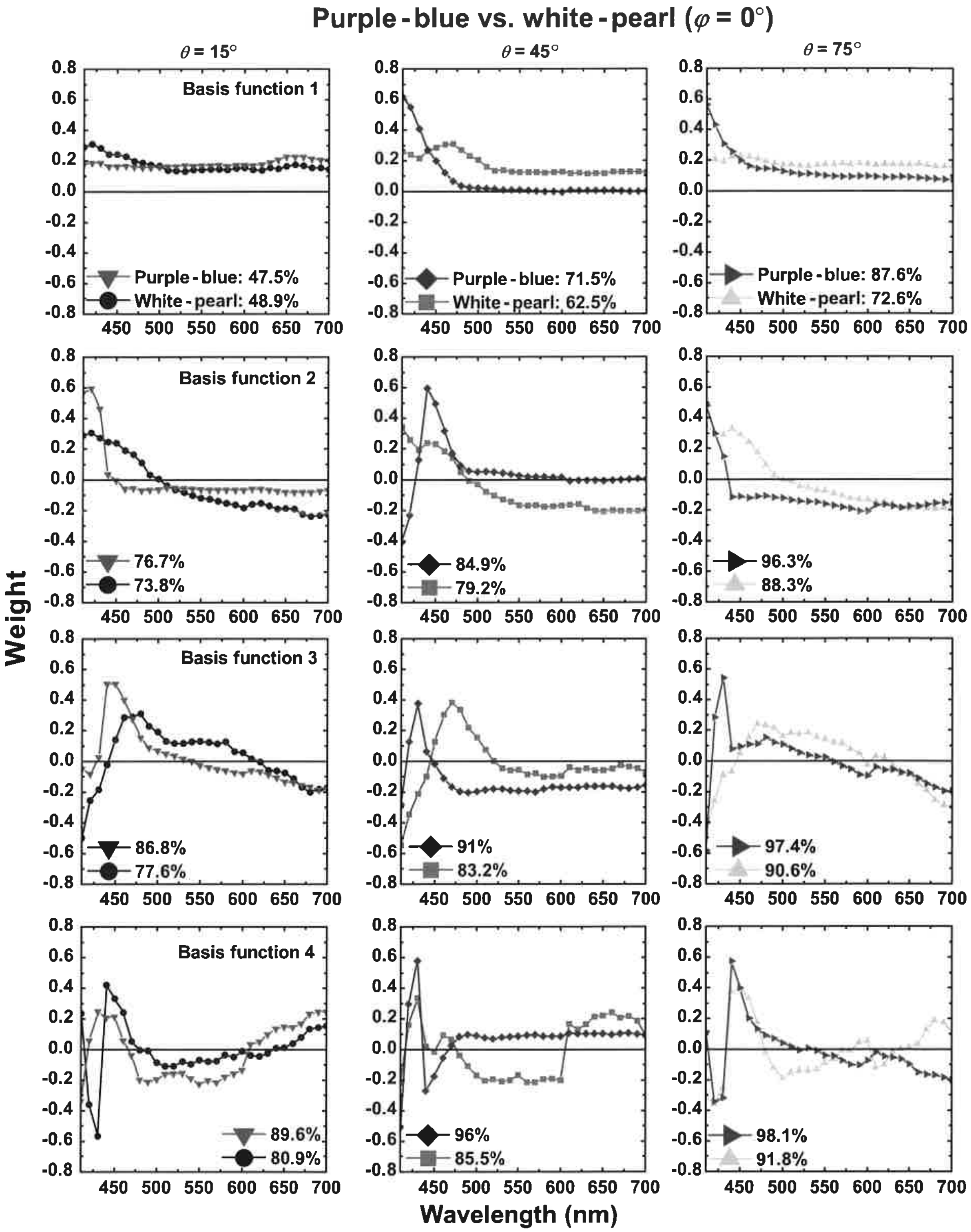

Fig. 8 The first four eigenvectors or basis functions of the purple-blue and white-pearl iridescent regions (angle $\varphi = 0$ deg) at the illumination angle θ of 15, 45, and 75 deg, separately. For each illumination angle, numbers indicate the cumulative percent of variance explained in the purple-blue and white-pearl wing scales.

containing the contribution of only one of the first four eigenvectors.

Reconstruction by using only the first eigenvector $\mathbf{S}_1$ contains most of the spatial details. They are different spatial patterns related to the bluish and whitish appearance of wing scales. Reconstruction by the next second eigenvector $\mathbf{S}_2$ shows weaker spatial patterns that are associated with the bluish-reddish and bluish-yellowish pigmentation of captured images. This could be associated with an irregular spatial distribution of melanin pigment in the wing scales.

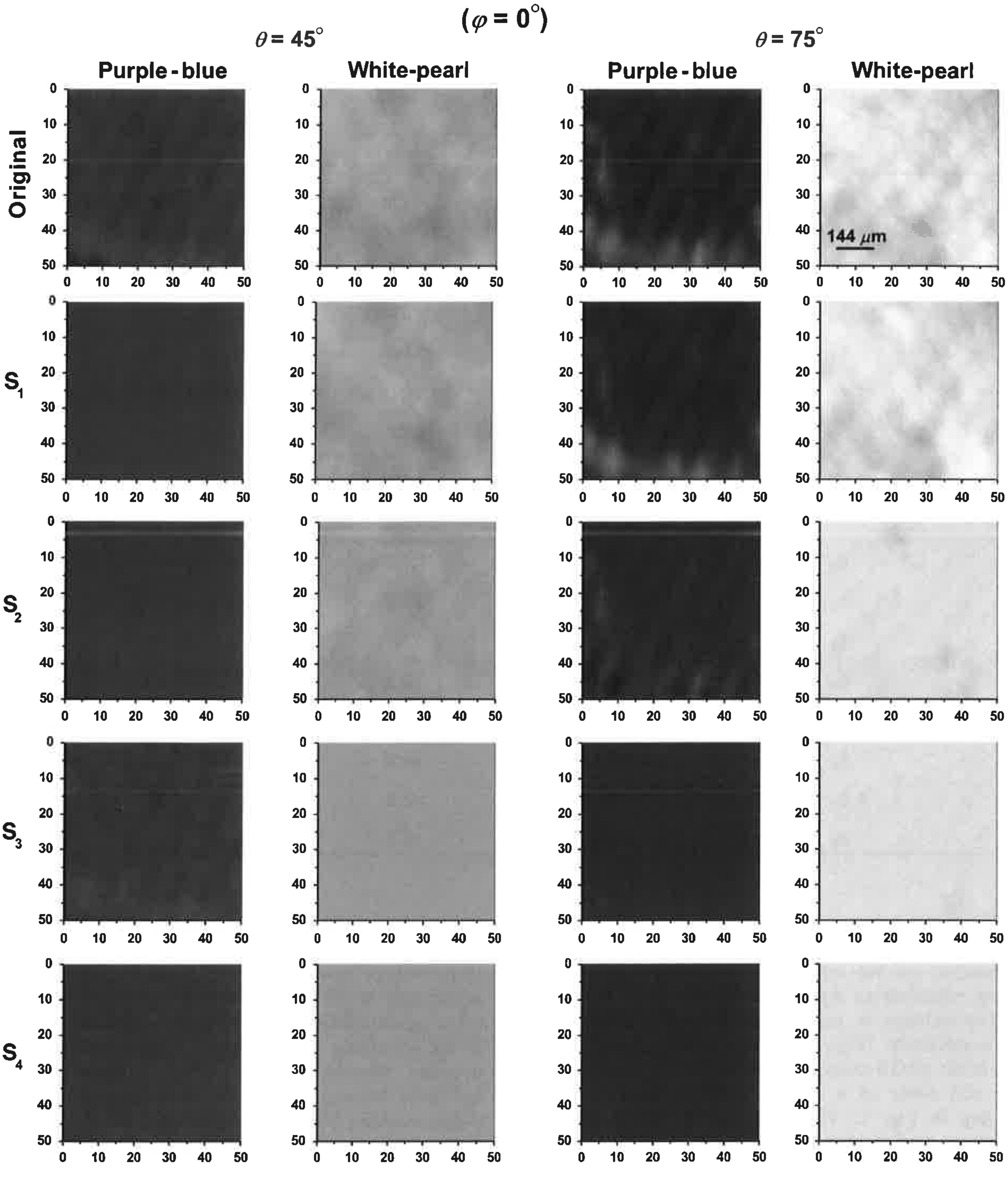

Fig. 9 Examples of reconstruction of purple-blue and white-pearl wing areas at the illumination angles $\theta = 45$ deg and $\theta = 75$ deg. Each panel indicates the reflectance spectra converted to color coordinates in the sRGB color space. The first row indicates the original purple-blue and white-pearl areas. Subsequent rows indicate the spatial distribution of the recovered reflectance spectra that results by the linear combination of the mean reflectance and one of the first four eigenvectors separately.

Two different forms of melanin are often associated with lepidopteran wing scales; eumelanin, a dark-brown pigment, and phenomelanin, a yellowish-reddish pigment.[21] The remaining two rows show the reconstruction by the third and fourth eigenvectors $\mathbf{S}_3$ and $\mathbf{S}_4$, respectively. They show even weaker spatial patterns suggesting the presence of irregular fluctuations or "noise."[40] In the purple-blue area at $\theta = 45$ deg, it is still possible to discern distinct whitish spatial patterns whereas at $\theta = 75$ deg and also in the white-pearl area, fluctuations around the mean reflectance in Eq. (2) are not visually discernable. Table 2 indicates the mean and maximum RMS-error between the original and recovered reflectances and the mean and maximum S-CIELAB ΔE color difference between the original and reconstructed RGB images.

Both mean and maximum RMS error and S-CIELAB ΔE values are lower when using the first eigenvector $\mathbf{S}_1$. All

Table 2 Mean, standard error of the mean (±1 SEM) and maximum (Max) RMS-error and S-CIELAB color difference of the reconstructed reflectance spectra from one of the first four eigenvectors.

		Purple-blue		White-pearl	
		RMS-error			
θ (deg)	Eigenvector	Mean (SEM)	Max	Mean (SEM)	Max
45	$\mathbf{S}_1$	0.119 (0.001)	0.362	0.124 (0.001)	0.363
	$\mathbf{S}_2$	0.196 (0.002)	0.819	0.177 (0.002)	0.542
	$\mathbf{S}_3$	0.207 (0.002)	0.859	0.192 (0.002)	0.544
	$\mathbf{S}_4$	0.209 (0.002)	0.858	0.194 (0.002)	0.543
75	$\mathbf{S}_1$	0.077 (0.001)	0.568	0.222 (0.002)	0.909
	$\mathbf{S}_2$	0.188 (0.004)	1.718	0.372 (0.004)	1.371
	$\mathbf{S}_3$	0.201 (0.004)	1.727	0.4048 (0.004)	1.364
	$\mathbf{S}_4$	0.201 (0.004)	1.737	0.4081 (0.004)	1.376
		S-CIELAB ΔE			
45	$\mathbf{S}_1$	3.49 (0.05)	15.47	4.35 (0.07)	23.44
	$\mathbf{S}_2$	5.72 (0.09)	24.9	4.54 (0.04)	12.9
	$\mathbf{S}_3$	7.1 (0.1)	25	5.88 (0.07)	23.44
	$\mathbf{S}_4$	7.1 (0.1)	24.6	5.72 (0.07)	21.7
75	$\mathbf{S}_1$	0.29 (0.01)	8.34	7.2 (0.1)	33.8
	$\mathbf{S}_2$	2.6 (0.1)	46.8	7.48 (0.09)	28.29
	$\mathbf{S}_3$	2.6 (0.1)	46.8	10.3 (0.1)	34.1
	$\mathbf{S}_4$	2.6 (0.1)	46.8	10.4 (0.1)	35

color differences between the original and reconstructed images are discernible in human color vision (Fig. 9). Reconstruction of the reflectance spectra by using the remaining eigenvectors represents <10.4% and 19.1% of cumulative variance in purple-blue and white-pearl wing scales, respectively (Fig. 8). Their spatial distributions mapped in the sRGB color space exhibit very weak spatial patterns and noise in a similar way as $\mathbf{S}_3$ and $\mathbf{S}_4$ at $\theta = 75$ deg in Fig. 9. This spatial noise arises due to many reasons and it may include noise from the spatial arrangement of wing scales. Those eigenvectors that explain a very small percentage of total variability may also indicate artifacts from the multispectral imaging system.[40,59]

4 Discussion

We have examined the components of the multispectral BRDF of the butterfly *S. charonda* in the visible range at different illumination and spatial positions. The spectral and colorimetric analysis in Figs. 5–7 demonstrate distinct angle-dependent color effects developed by purple-blue and white-pearl wing scales. Purple-blue scales enhance the blue coloring and they usually exhibit higher color saturation (Table 1). The absence of melanin is likely responsible for the whitish appearance of white-pearl scales in the *S. charonda*.[13,14] The lack of melanin may favor multiple light scattering that may be originated in the small irregularities in the photonic structure of wing scales and in the wing membrane. Consequently, background scattering may add white light to the bluish coherent scattering to reduce the color saturation (Fig. 5 and Table 1). This effect is similar to the whiteness effects found in the *E. mulciber*[10,12] and in various *Morpho* species such as in the *Morpho sulkowsky*[2] and in the *Morpho cypris*.[22] However, the blue iridescence of purple emperor butterflies differs from other species of lepidoptera due to variations in the cuticle-air layers piled on the ridges. For instance, the number of lamellae on the ridges in the *S. charonda* is higher than in the *E. mulciber*[10,12] and in the *A. meliboeus*,[9] whereas the tilt angle of cuticle-air layers is lower.[12–14] Blue coloring in purple emperor butterflies is associated with a blazed diffraction grating in the tilted cuticle-air lamellae on the ridges.[13–15,18] This is in contrast with the blue coloring produced in some species of *Morpho* butterflies that contain a number of lamellae similar to the *S. charonda* (e.g., *Morpho aega* and *Morpho aurora*).[20] In *Morpho* butterflies, blue structural color mainly originates by multilayer interference from the shelf structure of cuticles within the ridges.[1,2,6,20,25] Other structurally colored butterflies have developed alternative strategies to achieve distinct iridescent patterns in the UV-blue-green part of the spectrum by using different pigments. For instance, the combination of multilayer interference from cuticle-air stacks on the ridges and pterin pigments granules in the crossribs in various pierid species,[11,60] or the combination of a blazed diffraction grating from tilted multilayered microribs and fluorescent papiliochrome pigment in the papilionid *Troides magellanus*[10,12,61] are two remarkable examples.

All the results shown in Figs. 5–7 were done by averaging the reflectances over thousands of reflectance spectra obtained at different pixel locations. In this way, the multispectral imaging setup behaves in a similar manner to a conventional multiangle spectrophotometer that averages over small regions of interest of few millimeters[2,3,20,24] and reproduces the shape of reflectance spectra (Fig. 3). The strong blue coloring of the *S. charonda* has been explained by other workers as diffracted light occurring in the first order.[12–14] However, reflection patterns of these purple-blue wing scales are very different from those produced by manufactured diffraction gratings; contrary to the optical stop-band properties of multilayer systems, gratings generally disperse colors into different directions. The reflection patterns of *S. charonda*'s purple-blue scales do not show rainbow-like diffraction patterns; instead they exhibit vivid iridescence over a wide angular range,[12–14] in the same way as in *Morpho*-type structures.[1,2,6,20,25] The results in Figs. 4 and 5 show that iridescence from wing scales are captured within the numerical aperture of the multispectral system. The shape of the mean reflectance factor of the *S. charonda* is very similar to the purple emperor *A. ilia* and *A. iris* in the visible range.[15,19] A totally different aspect is to compare the BRDF obtained from the multispectral acquisition setup in Fig. 2 and that obtained with traditional spectroscopy methods. Multispectral BRDF imaging acquires 3-D data cubes at multiple illumination and spatial configurations; it contains more spatial information and is more sensitive to the orientation of wing scales and surface roughness (wing veins, hills, valleys, etc.). In the *S. charonda* this is clearly demonstrated in Figs. 4–6. However, in traditional spectroscopy methods minor spatial irregularities and defects are usually diluted within the imaged scene.[32,33]

Multispectral BRDF imaging has also a second advantage in the spatial reflectance mapping of iridescent tissue that other spectrophotometric methods do not have.[3,11,15,20,24,26,27] Our results show in Figs. 4, 8, and 9 that multispectral imaging can capture additional spectral and spatial information to examine at any pixel in the field of view, the spectral signature of purple-blue and white-pearl wing scales. This might allow more elaborate spatial reflectance models for classification and segmentation of iridescent tissue in bioimaging. In this sense, PCA is a robust standard method that it is widely used to classify multivariate spectral data and for noise reduction.[32,38–40] Reconstruction of reflectance spectra from PCA is appropriated to select those relevant eigenvectors that contribute to the spectral characteristics of iridescent tissue and to provide a better interpretation of principal components. By using PCA on multispectral BDRF data, we conclude that the number of eigenvectors or basis functions that provide >99% of cumulative variance is higher in white-pearl scales (Figs. 8 and 9 and Table 2). In accordance with Eq. (2), a higher number of basis functions in white-pearl scales indicate a higher number of dimensions and thus a higher spectral complexity in their spatial color pattern formation. Higher spectral complexity might be related in part with an irregular spatial distribution of melanin pigment across wing scales as suggested by the basis function 2 (Figs. 8 and 9). Other basis functions may also be related to melanin concentration differences across samples but their interpretation is less clear. Those basis functions that explain a very small percentage of variability are likely due to noise artifacts from the multispectral acquisition system and they could be discarded by projecting raw reflectance datasets onto those eigenvectors with large and medium variance in subsequent spectral modeling analyses.[40,59]

Multispectral BRDF data collected in the *S. charonda* are limited by the fact that the multispectral setup (Fig. 2) was restricted from 410 to 700 nm due to the lower transmission of the LCTF at low reflectance values at 400 nm (Fig. 3). The conclusions from the spectral and colorimetric analysis in Figs. 5–7 and Table 1 do not change when the values at 400 nm were excluded and PCA was already done by excluding reflectance data at 400 nm. The multispectral setup was developed by using optical components commercially available; its spectral calibration is standard and it was done by using a white diffuse reflectance standard.[51] However, the analysis of the multispectral BRDF of the *S. charonda* wing in the near-UV range may be implemented by using multispectral UV sensors. The modification of the current multispectral application to different spectral bands merits further investigation.

5 Conclusions

In summary, we report on the development of a novel multispectral acquisition system for the measurement of the BRDF of biological iridescent tissue in the visible range. Multispectral BRDF data were gathered by the combination of spectral and high-resolution spatial information with several illumination angles by using a goniometric setup. Therefore, multispectral BRDF imaging extends traditional multispectral reflectance imaging methods to multiple illumination and spatial positions and provides a considerable amount of spectral data; it also provides a valuable method of analyzing the spatial distribution of iridescence at the micron scale in the field of bioimaging and could have potential applications in histological analysis when iridescent tissues are analyzed in different liquids versus air.

In this paper, we have focused on the multispectral BRDF of the *S. charonda* purple-blue and white-pearl wing scales which have the same photonic structure and contain variable amounts of melanin pigment. Multispectral BRDF data were analyzed in user-defined regions of interest in many different ways, from mean spectral reflectance curves to factor analysis of reflectances at each pixel position. Reflectance spectra were also converted to color coordinates in appropriate color spaces for visual inspection as well as for quantitative colorimetric analysis. Spectral correlation analysis of reflectances obtained at different pixel positions was done by PCA. PCA results conclude that the number of basis functions necessary to achieve >99% of cumulative variance was higher in white-pearl wing scales. This suggests a higher spectral complexity in their spatial color pattern organization. Although we have exemplified the measurement of the multispectral BRDF in the study of the *S. charonda* butterfly wing, it could be applied to other structurally colored butterfly wings as well as in the research on iridescence and possible damage in the scales, eyes, and skin of animals reflectors such as skin iridescence in fishes, squids, and birds, iridescence in the cornea of many fishes or in the *tapetum lucidum* in the retina of many vertebrate animals (e.g., cat's eye).

Acknowledgments

This research was developed during a visiting research stay of Dr. José M. Medina in the Departmento de Óptica, Universidad de Granada, Spain. This work was supported by the Departmento de Óptica, Universidad de Granada. We thank the Servicio de Microscopia, Centro de Instrumentación Científica, Universidad de Granada, and Dr. David Porcel Muñoz for technical assessment and Fig. 1(c). J.M.M. and J.A.D. acknowledge the European Regional Development Fund—ERDF through Programa Operacional Factores de Competitividade—COMPETE (FCOMP-01-0124-FEDER-014588), and the National Portuguese funds through the Fundação para a Ciência e Tecnologia—FCT (PTDC/CTM-MET/113352/2009). P.V. acknowledges USAF funding (Award No. FA9550-10-1-0020).

References

1. P. Vukusic and J. R. Sambles, "Photonic structures in biology," *Nature* **424**(6950), 852–855 (2003).
2. S. Kinoshita, S. Yoshioka, and J. Miyazaki, "Physics of structural colors," *Rep. Prog. Phys.* **71**(7), 76401–76431 (2008).
3. L. P. Biro and J. P. Vigneron, "Photonic nanoarchitectures in butterflies and beetles: valuable sources for bioinspiration," *Laser Photonics Rev.* **5**(1), 27–51 (2011).
4. P. Vukusic, J. R. Sambles, and H. Ghiradella, "Optical classification of microstructure in butterfly wingscales," *Photonics Sci. News* **6**, 61–66 (2000).
5. H. Ghiradella, "Structure of iridescent lepidopteran scales: variations on several themes," *Ann. Entomol. Soc. Am.* **77**(6), 637–645 (1984).
6. P. Vukusic et al., "Quantified interference and diffraction in single Morpho butterfly scales," *Proc. R. Soc. Lond. B* **266**(1427), 1403–1411 (1999).
7. H. Ghiradella, "Light and color on the wing: structural colors in butterflies and moths," *Appl. Opt.* **30**(24), 3492–3500 (1991).
8. H. Ghiradella et al., "Ultraviolet reflection of a male butterfly: interference color caused by thin-layer elaboration of wing scales," *Science* **178**(4066), 1214–1217 (1972).
9. P. Vukusic et al., "Structural colour—now you see it now you don't," *Nature* **410**(6824), 36–36 (2001).
10. P. Dechkrong et al., "Fine structure of wing scales of butterflies, Euploea mulciber and Troides aeacus," *J. Struct. Biol.* **176**(1), 75–82 (2011).
11. B. Wilts, P. Pirih, and D. Stavenga, "Spectral reflectance properties of iridescent period butterfly wings," *J. Comp. Physiol. A* **197**(6), 693–702 (2011).
12. F. Mika et al., "Photonic crystal structure and coloration of wing scales of butterflies exhibiting selective wavelength iridescence," *Materials* **5**(5), 754–771 (2012).
13. J. Matějková-Plšková, S. Shiojiri, and M. Shiojiri, "Fine structures of wing scales in Sasakia charonda butterflies as photonic crystals," *J. Micros.* **236**(2), 88–93 (2009).
14. J. Matějková-Plšková et al., "Photonic crystal structure of wing scales in Sasakia charonda butterflies," *Mater. Trans.* **51**(2), 202–208 (2010).
15. D. Pantelić et al., "High angular and spectral selectivity of purple emperor (Lepidoptera: Apatura iris and A. ilia) butterfly wings," *Opt. Express* **19**(7), 5817–5826 (2011).
16. V. B. Meyer-Rochow and E. Eguchi, ""Flugelfarben,wie sie die Falter sehen"—a study of UV-and other colour patterns in Lepidoptera," *Annot. Zool. Jpn.* **56**(2), 85–99 (1983).
17. E. Eguchi and V. B. Meyer-Rochow, "Ultraviolet photography of forty-three species of lepidoptera representing ten families," *Annot. Zool. Jpn.* **56**(1), 10–18 (1983).
18. S. B. Ćurčić et al., "Micro- and nanostructures of iridescent wing scales in purple emperor butterflies (Lepidoptera: Apatura ilia and A. iris)," *Microsc. Res. Tech.* **75**(7), 968–976 (2012).
19. Z. W. Han et al., "Structural colour in butterfly Apatura ilia scales and the microstructure simulation of photonic crystal," *J. Bionic Eng.* **5**(Suppl. 1), 14–19 (2008).
20. S. Berthier, E. Charron, and J. Boulenguez, "Morphological structure and optical properties of the wings of Morphidae," *Insect Sci.* **13**(2), 145–157 (2006).
21. G. Zonios and A. Dimou, "Melanin optical properties provide evidence for chemical and structural disorder in vivo," *Opt. Express* **16**(11), 8263–8268 (2008).
22. S. Yoshioka and S. Kinoshita, "Structural or pigmentary? Origin of the distinctive white stripe on the blue wing of a Morpho butterfly," *Proc. R. Soc. B* **273**(1583), 129–134 (2006).
23. F. E. Nicodemus, "Directional reflectance and emissivity of an opaque surface," *Appl. Opt.* **4**(7), 767–773 (1965).
24. P. Vukusic and D. G. Stavenga, "Physical methods for investigating structural colours in biological systems," *J. R. Soc. Interface* **6**(Suppl. 2), S133–S148 (2009).
25. B. Gralak, G. Tayeb, and S. Enoch, "Morpho butterflies wings color modeled with lamellar grating theory," *Opt. Express* **9**(11), 567–578 (2001).
26. S. E. Mann, I. N. Miaoulis, and P. Y. Wong, "Spectral imaging, reflectivity measurements, and modeling of iridescent butterfly scale structures," *Opt. Eng.* **40**(10), 2061–2068 (2001).
27. D. G. Stavenga et al., "Imaging scatterometry of butterfly wing scales," *Opt. Express* **17**(1), 193–202 (2009).
28. Y. Sun, "Rendering biological iridescences with RGB-based renderers," *ACM Trans. Graph.* **25**(1), 100–129 (2006).
29. N. Okada et al., "Rendering Morpho butterflies based on high accuracy nano-optical simulation," *J. Opt.* **42**(1), 25–36 (2013).
30. N. Gat, "Imaging spectroscopy using tunable filters: a review," *Proc. SPIE* **4056**, 50 (2000).
31. J. Y. Hardeberg, F. Schmitt, and H. Brettel, "Multispectral color image capture using a liquid crystal tunable filter," *Opt. Eng.* **41**(10), 2532–2548 (2002).
32. H. F. Grahn and P. Geladi, *Techniques and Applications of Hyperspectral Image Analysis*, John Wiley & Sons Ltd., Chichester, England (2007).
33. Q. Li et al., "Review of spectral imaging technology in biomedical engineering: achievements and challenges," *J. Biomed. Opt.* **18**(10), 100901 (2013).
34. J. Medina, S. Nascimento, and P. Vukusic, "Hyperspectral optical imaging of two different species of lepidoptera," *Nanoscale Res. Lett.* **6**(369), 1–5 (2011).
35. M. Tsuchida et al., "Development of BRDF and BTF measurement and computer-aided design systems based on multispectral imaging," in *Proc. AIC Colour 05*, Vol. 1, pp. 129–132, International Colour Association, Granada, Spain (2005).
36. A. Kimachi, N. Tanaka, and S. Tominaga, "Development and calibration of a goniospectral imaging system for measuring surface reflection," *IEICE Trans. Inf. Syst.* **E89-D**(7), 1994–2003 (2006).
37. D. B. Kim et al., "Acquisition and representation of pearlescent paints using an image-based goniospectrophotometer," *Opt. Eng.* **49**(4), 043604 (2010).
38. I. T. Jolliffe, *Principal Component Analysis*, Springer-Verlag, New York (2002).
39. D. Y. Tzeng and R. S. Berns, "A review of principal component analysis and its applications to color technology," *Color Res. Appl.* **30**(2), 84–98 (2005).
40. P. Bajorski, *Statistics for Imaging, Optics, and Photonics*, John Wiley & Sons, Hoboken, New Jersey (2012).
41. N. Ohta, "Estimating absorption-bands of component dyes by means of principal component analysis," *Anal. Chem.* **45**(3), 553–557 (1973).
42. X. Jiang et al., "Investigation on color variation of Morpho butterfly wings hierarchical structure based on PCA," *Sci. China Technol. Sci.* **55**(1), 16–21 (2012).
43. R. A. Potyrailo et al., "Morpho butterfly wing scales demonstrate highly selective vapour response," *Nat. Photonics* **1**(2), 123–128 (2007).
44. R. A. Potyrailo et al., "Discovery of the surface polarity gradient on iridescent Morpho butterfly scales reveals a mechanism of their selective vapor response," *Proc. Natl. Acad. Sci. U. S. A.* **110**(39), 15567–15572 (2013).
45. J. M. Medina and J. A. Díaz, "Scattering characterization of nanopigments in metallic coatings using hyperspectral optical imaging," *Appl. Opt.* **50**(31), G47–G55 (2011).
46. M. A. López-Álvarez et al., "Calibrating the elements of a multispectral imaging system," *J. Imaging Sci. Technol.* **53**(3), 031102 (2009).
47. J. Beeckman, K. Neyts, and P. J. M. Vanbrabant, "Liquid-crystal photonic applications," *Opt. Eng.* **50**(8), 081202 (2011).
48. G. Wyszecki and W. S. Stiles, *Color Science: Concepts and Methods, Quantitative Data and Formulae*, John Wiley & Sons, New York (1982).
49. G. A. Klein, *Industrial Color Physics*, Springer Science+Business Media LLC, New York (2010).
50. G. E. Healey and R. Kondepudy, "Radiometric CCD camera calibration and noise estimation," *IEEE Trans. Pattern Anal. Mach. Intell.* **16**(3), 267–276 (1994).
51. Labsphere, "Spectralon diffuse reflectance standards," (2011), http://www.labsphere.com/uploads/datasheets/diffusereflectance-standards-product-sheet.pdf (16 November 2010).

52. R. A. Yotter and D. M. Wilson, "A review of photodetectors for sensing light-emitting reporters in biological systems," *IEEE Sens. J.* **3**(3), 288–303 (2003).
53. M. Anderson et al., "Proposal for a standard default color space for the Internet—sRGB," in *Proc. IS&T/SID Fourth Color Imaging Conf.*, pp. 238–246, Imaging Science and Technology, Scottsdale, Arizona (1996).
54. C. S. McCamy, H. Marcus, and J. G. Davidson, "A color-rendition chart," *J. Appl. Photogr. Eng.* **2**(3), 95–99 (1976).
55. N. Ohta, "The basis of color reproduction engineering," Munsell Color Science Laboratory (1997), http://www.cis.rit.edu/research/mcsl2/online/cie.php (1 April 2002).
56. X. Zhang and B. A. Wandell, "A spatial extension of CIELAB for digital color-image reproduction," *J. Soc. Inf. Disp.* **5**(1), 61–63 (1997).
57. X. Zhang and B. A. Wandell, "Introduction to S-CIELAB," (1998), http://white.stanford.edu/~brian/scielab/ (18 May 1998).
58. J. M. Medina, "Linear basis for metallic and iridescent colors," *Appl. Opt.* **47**(30), 5644–5653 (2008).
59. J. M. Lopez-Alonso and J. Alda, "Characterization of scenarios for multiband and hyperspectral imagers," *Proc. SPIE* **5439**, 140 (2004).
60. N. I. Morehouse, P. Vukusic, and R. Rutowski, "Pterin pigment granules are responsible for both broadband light scattering and wavelength selective absorption in the wing scales of pierid butterflies," *Proc. R. Soc. B* **274**(1608), 359–366 (2007).
61. J. P. Vigneron et al., "Correlated diffraction and fluorescence in the backscattering iridescence of the male butterfly Troides magellanus (Papilionidae)," *Phys. Rev. E* **78**(2), 021903 (2008).

Biographies of the authors are not available.